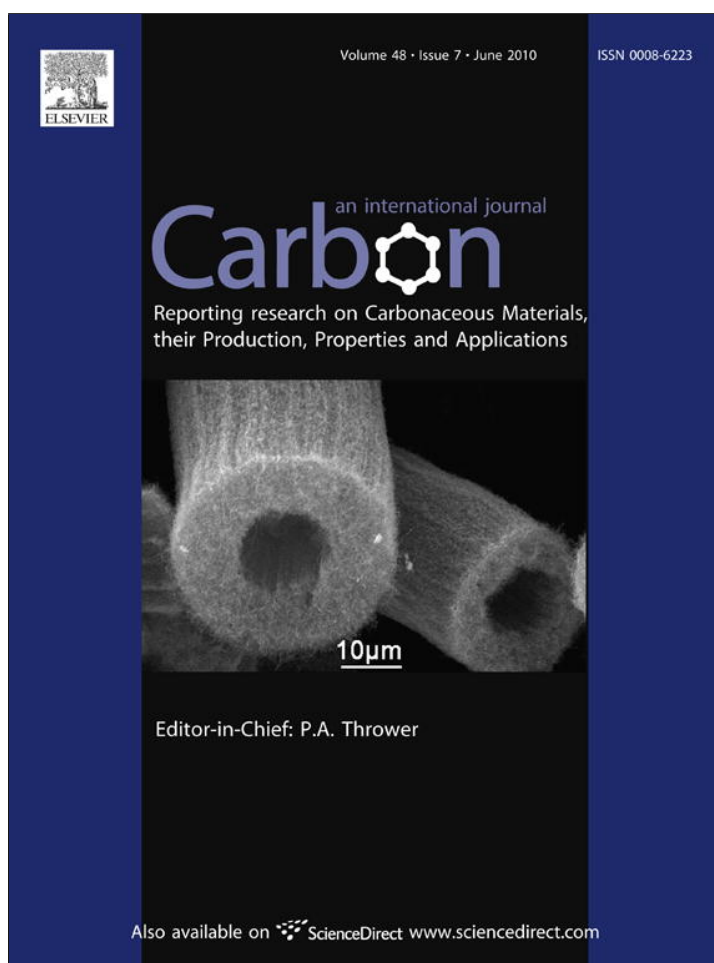


Provided for non-commercial research and education use.  
Not for reproduction, distribution or commercial use.

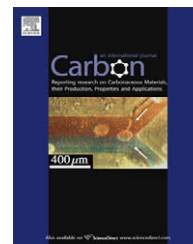


This article appeared in a journal published by Elsevier. The attached copy is furnished to the author for internal non-commercial research and education use, including for instruction at the authors institution and sharing with colleagues.

Other uses, including reproduction and distribution, or selling or licensing copies, or posting to personal, institutional or third party websites are prohibited.

In most cases authors are permitted to post their version of the article (e.g. in Word or Tex form) to their personal website or institutional repository. Authors requiring further information regarding Elsevier's archiving and manuscript policies are encouraged to visit:

<http://www.elsevier.com/copyright>

available at [www.sciencedirect.com](http://www.sciencedirect.com)journal homepage: [www.elsevier.com/locate/carbon](http://www.elsevier.com/locate/carbon)

# Catalytic oxidation kinetics of iron-containing carbon particles generated by spraying ferrocene-mixed with diesel fuel into a hydrogen–air diffusion flame

Yong Ho Kim <sup>a</sup>, Yong-Tae Kim <sup>a</sup>, Soo Hyung Kim <sup>b</sup>, Donggeun Lee <sup>a,\*</sup>

<sup>a</sup> School of Mechanical Engineering, Pusan Clean Coal Center, Pusan National University, San 30, Jangjeon Dong, Geumjeong Gu, Busan 609-735, South Korea

<sup>b</sup> Department of Nanosystem and Nanoprocess Engineering, College of Nanoscience and Nanotechnology, Pusan National University, Chunghak-Li 50, Samryangjin-Eup, Milyang-Si, Gyungnam-Do 627-706, South Korea

## ARTICLE INFO

### Article history:

Received 23 September 2009

Accepted 11 February 2010

Available online 15 February 2010

## ABSTRACT

Kinetic measurements of the catalytic oxidation of iron-containing soot particles were made for a better understanding of the role of catalytic particles in the initiation of soot oxidation. Carbon-based iron-containing soot particles were generated by spraying ferrocene-mixed with diesel fuel into an oxy-hydrogen flame. A commercial carbon black was used as a standard. Their oxidative kinetics and physico-chemical characteristics were measured by thermogravimetric analysis, secondary ion mass spectrometry, X-ray diffraction, gas-cell Fourier-transform infrared spectroscopy, induced coupled plasma-atomic emission spectroscopy, and high-resolution transmission electron microscopy. It was found that a tiny amount of ferrocene led to a significant reduction in both the on-set temperature and the activation energy of soot oxidation. Catalytic oxidation occurred in two consecutive steps, as temperature increased. The initiation of oxidation, even with an addition of ferrocene, was controlled mainly by surface oxygen complexes and partly by the long-range crystalline order of the carbon graphene layer. However, once catalytic oxidation began, the progress of the reaction was mainly determined by the amount of ferrocene that was added.

© 2010 Elsevier Ltd. All rights reserved.

## 1. Introduction

The diesel particulate filter (DPF) suggested in response to strengthened regulation [1–4] experiences a gradual accumulation of particulate matters (PM), leading to increase in the back pressure of the cylinder, degrading engine performance. Therefore, there is an urgent need for continuous or intermittent regeneration of the DPF, which has initiated various researches, starting with “forced regeneration” using an external heating source such as electricity or hydrocarbon fuel, to the development of efficient catalysts targeting a

reduction in the oxidation temperature of the PM up to exhaust gas temperature of the diesel engine [5–8].

Various transition metal oxides have therefore been tested as less expensive catalysts [5–8]. Setzer et al. [9] ranked the oxides of Cu, Fe and Co as more active catalysts compared to Ni and Zn. Neef et al. [5] investigated five types of metal oxides and ordered them by catalytic activity as Co > V > Fe > La > Mn > Ni. As the catalytic performance was greatly influenced by the degree of physical contact between the catalysts and the PM [5,6], various fuel additives have been considered as a source of fuel-borne catalysts that

\* Corresponding author. Fax: +82 51 512 5236.

E-mail address: [donglee@pusan.ac.kr](mailto:donglee@pusan.ac.kr) (D. Lee).

0008-6223/\$ - see front matter © 2010 Elsevier Ltd. All rights reserved.

doi:10.1016/j.carbon.2010.02.018

maximize this mutual contact [1,10–12]. Excluded are Cu- and Pb-containing additives, as they emit hazardous secondary pollutants such as dioxin or lead. On the other hand, Ce- or Fe-based additives are promising candidates.

Lahaye et al. [1], who used a diesel fuel mixed with 2500–5000 ppm cerium octoate, reported that the on-set temperature of PM oxidation was reduced from 500 to 375 °C at 0.3 wt.% of Ce content in the PM. However, further mixing of the Ce precursor increased the temperature to 450 °C, even with a reduction of the activation energy for PM oxidation from 170 to 120 kJ mol<sup>-1</sup>. Stanmore et al. [11] observed the highest reaction rate at 3.6–6.9 wt.% of Ce content with an invariant activation energy of approximately 210 kJ mol<sup>-1</sup>. Such a large discrepancy in the data turned our attention to an iron-based catalyst, as this was expected to show a better catalytic effect and less adverse health effects compared to cerium [5] as well as less emission of PM from an engine. This can offer a prolonged regeneration period for a DPF [4,13,14]. For this reason, ferrocene ((C<sub>5</sub>H<sub>5</sub>)<sub>2</sub>Fe) is employed as an iron source in this study. Only limited studies have been reported in this area. Examples include the monitoring of the auto-thermal regeneration in a DPF-employed diesel vehicle [4], reduced generation of PM in the cylinder [14], an investigation of the oxidation kinetics of carbon-based aerosol using a tandem differential mobility analyzer [13,15], and a formation mechanism for metal-containing catalytic particles [16].

Here, the physical and chemical properties of iron-containing PM are identified through various characterization methods. Dynamic and isothermal thermogravimetric analyses were done separately in an effort to examine the reaction kinetics of iron-containing PM with different doping levels of ferrocene and surface treatments of the PM samples. It was found that a tiny amount of ferrocene led to a significant reduction in both the on-set temperature and the activation energy of soot oxidation. Attempts were made to correlate the enhanced kinetic parameters with surface-reactive species of the PM such as the surface oxygen complexes (SOC) and the crystalline order of the carbon graphene layer (CGL). The objective of the present study is therefore to provide data pertaining to the physico-chemical characteristics of catalyzed PM in comparison with the oxidation kinetics and then to identify the significant factors of the catalytic oxidation process as well as a possible mechanism.

## 2. Experiment

### 2.1. Synthesis and sampling of iron-containing PM

In this study, an oxy-hydrogen diffusion flame was employed as a heat source to pyrolyze a ferrocene-mixed diesel fuel. Fig. 1 shows a schematic of the flame burner, which consists of five concentric tubes. Hydrogen (1.5 l min<sup>-1</sup>) and oxygen (5.0 l min<sup>-1</sup>) are supplied through the second and fourth tubes, respectively. The initial concentration of ferrocene in the diesel fuel was adjusted to 0, 50, 500, and 1500 ppm. The concentration will be referred as mixing level hereafter. The fuel mixture is nebulized to 1–5 μm droplets by compressed argon gas (2.5 × 10<sup>6</sup> Pa) and then fed into the center tube with an argon flow of 0.68 l min<sup>-1</sup>. The tube is heated at 100 °C to

prevent recondensation of the vaporized fuel. Argon is used as carrier gas to pyrolyze fuel vapors in the low-oxygen environment. Nitrogen gas flows through the third tube at a flow rate of 0.5 l min<sup>-1</sup> to control flame temperature and the local fuel–air ratio. The flame is stabilized by flowing 40 l min<sup>-1</sup> of argon through the outermost tube in which a honeycomb, a fine metal mesh and glass bead are incorporated. As shown in Fig. 1, a quartz tube cooled by tap water is placed horizontally above the flame for thermophoretic sampling of the PM. It moves back and forth by a pneumatic cylinder.

The aforementioned flow rates of the gases were determined for the maximum generation of PM from many tests involving a variety of combinations of gas flow rates and gas injection positions. Additional details of the burner and the sampling apparatus are available in the literature [17]. Diesel fuel used in this study was provided by Hyundai Oilbank in Korea, the composition of which is similar to EPA No. 2 on-road diesel fuel except of its much lower sulfur content (refer to Table 1 for physico-chemical properties of the diesel fuel). Acetylene was initially tested as a carbon source by injecting acetylene into a hydrogen–air diffusion flame. However, only fraction of the flame soot particles was covered with Fe-containing catalysts, suggesting that acetylene flame generates continuously carbon particles even after ferrocene decomposition ends. Direct spraying of diesel fuels blended with ferrocene is therefore considered for coincident formation of soot and iron species, and easy control of the iron content in soot particles as well. This will be confirmed later.

### 2.2. Characterizations and kinetic measurements of iron-catalyzed PM

Thermogravimetric analysis (TGA; Q50, TA Instrument) was used to measure the on-set temperature, reaction rates, and activation energies of oxidation of PM produced with four different content levels of ferrocene. A commercial carbon black (CB) powder (Printex-U, Degussa) was also used as a standard for comparison of the oxidation characteristics because the physico-chemical properties of CB are well known as a result of extensive studies since 1990; C: 97.23, H: 0.73, O: 1.16, N: 0.19, S: 0.45 wt.%; specific surface area of 96 m<sup>2</sup> g<sup>-1</sup> and a mean size of 80–250 nm [2,5,6,8,12,18–22]. It was found that the TGA profiles were reproducible for several tests with different initial sample masses ranging from 2 to 8 mg, suggesting that heat/mass transfer-related artifacts are negligible [23]. A further discussion on the transport related artifacts is made from the following simple estimation. A Pt sample pan with 7 mm in diameter (D) and 3 mm in depth (h) was used for TGA measurements. A few milligram of sample was apparently spread as a single layer with a thickness of less than 0.5 mm (t) on the bottom of the pan. Two thermocouples were installed on the sample pan and right above the sample in Q50 TGA machine, in an effort to reduce the heat transfer artifact. The closest distance (L) between the second thermocouple and pan is ca. 2 mm. The characteristic time for heat transfer can be estimated by the time of heat conduction from sample pan, through the powder layer, to the thermocouple:  $L^2/\alpha_{\text{layer}}$ . The thermal diffusivity of porous sample layer  $\alpha_{\text{layer}}$  is estimated to  $1.01 \times 10^{-4} \text{ m}^2 \text{ s}^{-1}$  by  $\alpha_{\text{layer}} = (1 - f) \times \alpha_{\text{air}} + f \times \alpha_{\text{graphite}}$  provided a solid volume

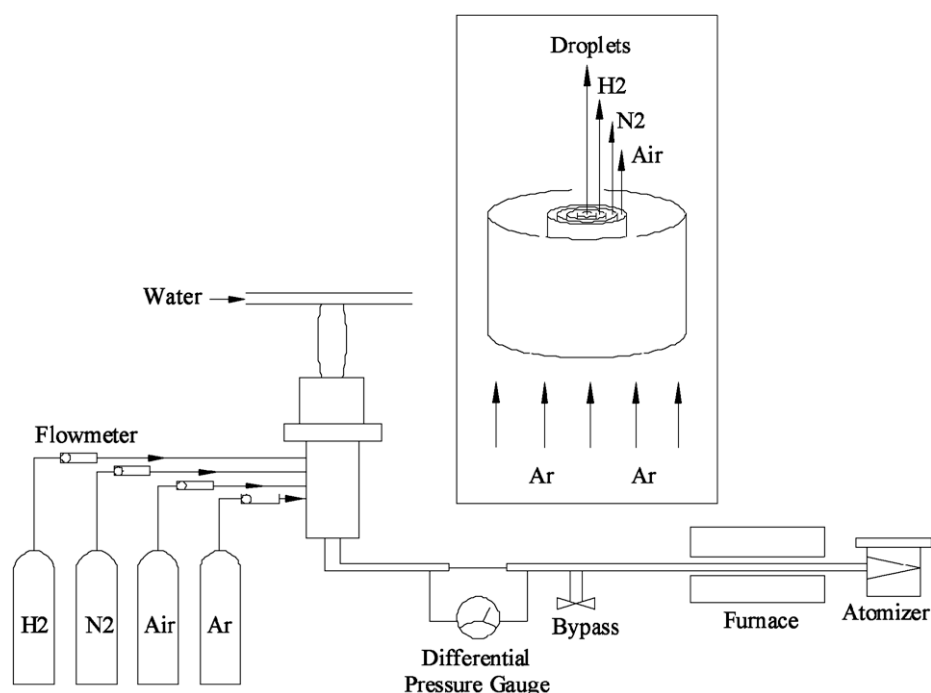


Fig. 1 – A schematic of hydrogen–air diffusion flame burner employed in the present research and particle capturing tube.

Table 1 – Physicochemical properties of diesel fuel used in this study.

Properties	HDO-Diesel	
Pour point (°C)	<0.0	
Flash point (°C)	>40	
Kinematic viscosity (at 40 °C, mm <sup>2</sup> s <sup>-1</sup> )	1.9–5.5	
Distillation (90 vol.%, °C)	<360	
Sulfur (ppm)	<30	
Ash (wt.%)	<0.02	
Cetane index	>45	
Density at 15 °C (kg m <sup>-3</sup> )	815–855	
Metal contents from ICP-AES (100 × ppm)	Fe	5.819
	Na	41.118
	Ca	23.356
	K	12.195

fraction ( $f$ ) of 4.6%. The characteristic time for heat conduction is then calculated to less than 0.04 s and the characteristic time for mass transfer is similarly calculated to  $\sim 0.1$  s by  $h^2/D_{CO_2}$  where  $D_{CO_2}$  is a diffusion coefficient of product gas CO<sub>2</sub> at 400 °C ( $\sim 8.9 \times 10^{-5}$  m<sup>2</sup> s<sup>-1</sup>). As the two times are both much shorter than the time for heating the sample by 1 °C (15 s = 1/4 °C min<sup>-1</sup>), any artifacts for heat and mass transfer are believed to be negligible.

Iron-containing PM from a flame was deposited onto a transmission electron microscopy (TEM) grid using a local thermophoretic sampler [17] for 0.2 s. The sampling position of the grid was adjusted by a precision X–Y stage. The morphology and size of the as-prepared PM samples were observed with TEM (H-7600, Hitachi) running at an acceleration voltage of 200 kV. Energy dispersive spectroscopy (EDS; attached to the TEM machine) was used in conjunction

with TEM to investigate the composition of iron-containing species over the PM. The microstructure and crystalline phase of the iron-containing PM agglomerates were also observed with high-resolution TEM (HR-TEM; JEM-2100F, Jeol).

A gas-cell Fourier-transform infrared spectroscopy (GC-FTIR, Nicolet 380, Thermo Electron) was employed to analyze composition of the various gases that evolved from the oxidation of PM in real time. A weighed PM sample was put into a small alumina boat in a tubular furnace set at 300 °C. The gases that evolved from the sample, under flowing dry air at 1 l min<sup>-1</sup>, were introduced to the GC-FTIR. The GC-FTIR spectrum of each sample was scanned 32 times with a resolution of 4 cm<sup>-1</sup> in the range of 1000–4000 cm<sup>-1</sup> and these values were then averaged. A calibration experiment was performed for a quantitative assignment of the major evolving gas CO<sub>2</sub>. It was confirmed that the CO<sub>2</sub> peaks at  $\sim 2360$  cm<sup>-1</sup> and 3700–3800 cm<sup>-1</sup> increased quite linearly with the increase in the flow rate of CO<sub>2</sub> from 2.5% to 15% at the constant air flow rate.

An X-ray diffraction (XRD; D/Max-2499, Rigaku) analysis was conducted to observe any changes in the crystallite size of the carbon particles as the mixing level of ferrocene increased. XRD patterns were obtained by scanning the PM sample in the  $2\theta$  range of 10–90° at 4° min<sup>-1</sup> using a Cu K $\alpha$  X-ray source (30 kV, 40 mA, 1.5418 Å). In addition, a Micro-Raman spectrometer (inVia Raman Microscope, Renishaw) was used to identify defect structures of carbon spherules in the catalyzed- and un-catalyzed-PM agglomerates. A tiny PM sample of  $\sim 10$  μm in diameter was scanned in the Raman-shift range of 1000–1900 cm<sup>-1</sup> at a resolution of 2 cm<sup>-1</sup>.

Metallic elements in the PM were analyzed quantitatively using induced coupled plasma-atomic emission spectroscopy (ICP-AES; JY-ULTIMA 2CHR, Horiba JY) operating at a radio-frequency of 40.68 MHz and 1000 W of power. Surface species of PM agglomerates were analyzed by secondary

ion mass spectroscopy (SIMS; PHI-7200, Perkin-Elmer) with irradiation of energetic Cs ion of 8 keV.

### 3. Results and discussion

#### 3.1. Effect of ferrocene on soot formation in a flame

Fig. 2(a1–a3) show the evolution of soot particles in the flame in the absence of ferrocene, starting from the large cloud-like condensed phase likely corresponding to polycyclic aromatic hydrocarbon (PAH) in Fig. 2(a1), followed by the formation of dark spots representing the inception of carbonaceous soot

in Fig. 2(a2) and subsequent growth to mature soot aggregates in Fig. 2(a3). Similar behavior was observed in the sooting region of an ethane inverse diffusion flame [24]. In comparison to Fig. 2(a1–a3) and (b1–b3) show that even a tiny amount of ferrocene, such as 50 ppm, if added to diesel fuel, apparently accelerates the fuel-to-soot conversion process. Comparing Fig. 2(b3–a3), the agglomerates clearly become smaller in the presence of ferrocene, though their primary particle sizes are almost invariant; the mean size of agglomerates decreases from 367 to 179 nm while the standard deviation representing the polydispersity is hardly varied (from 84 to 76 nm), respectively. Therefore, ferrocene manifestly

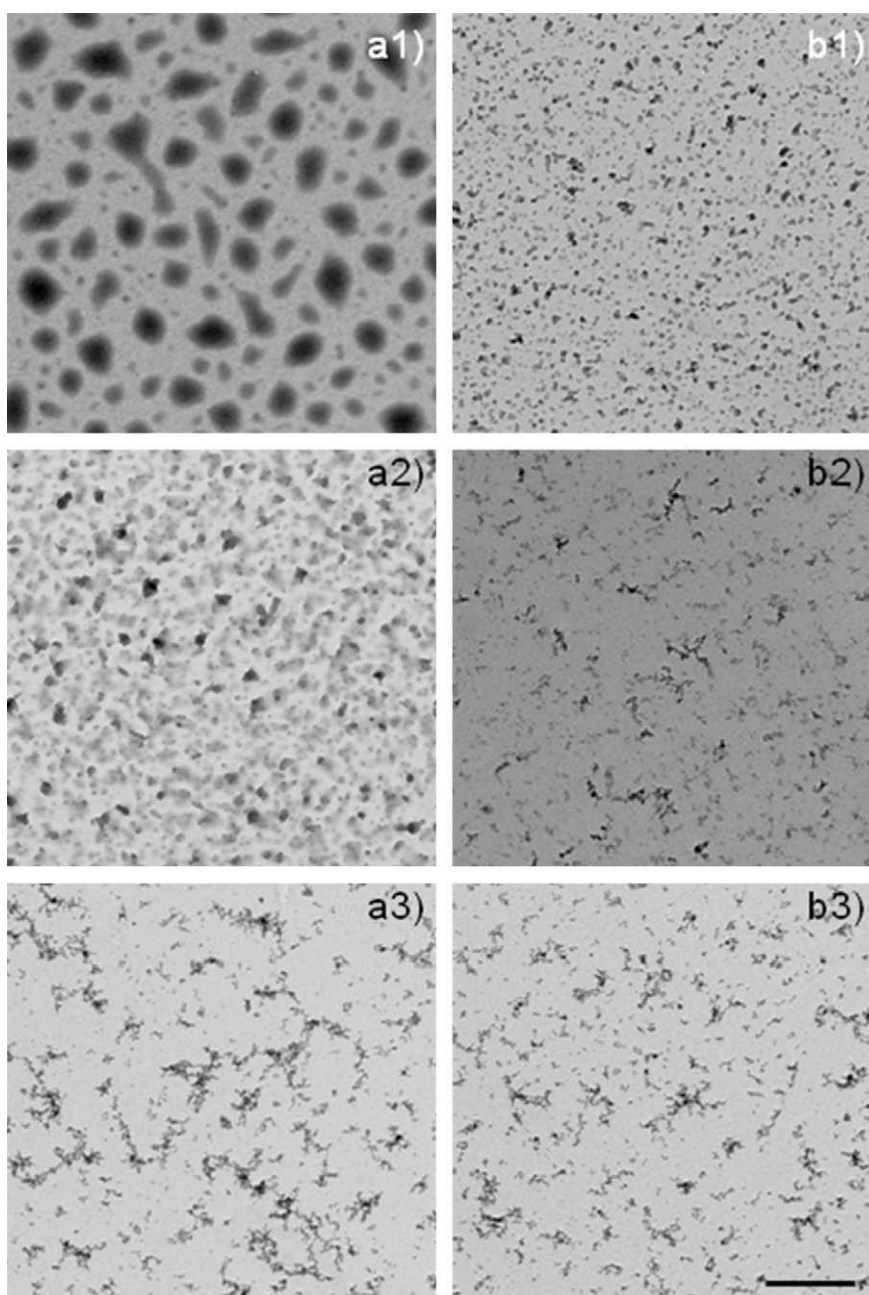


Fig. 2 – Evolution of soot particles in the flame: the left-side and right-side figures correspond to 0 and 50 ppm of ferrocene doping, respectively, while the numbers of 1, 2, and 3 represent flame heights at which particles are deposited such as 66, 76, and 86 mm, respectively. The bar represents 500 nm.

promotes the entire process of the combustion of vaporized liquid fuel, soot inception, and final oxidation of the soot particles.

Fig. 3(a) shows a TEM image of iron-containing carbon agglomerates captured at a height of 86 mm and at a dose of 50 ppm ferrocene. The vicinity of a dark spot in the image is magnified in Fig. 3(b), showing that the dark spot is a crystalline material. The dark spot, B, and its surrounding area, A, in Fig. 3(b) were analyzed by EDS. These results are shown in Fig. 3(d and c), respectively, revealing that the dark spot B is likely composed of iron compounds or metallic iron, presumably generated from the pyrolysis and/or oxidation of ferrocene. Si and Cu peaks come from the SiO<sub>2</sub>-coated Cu TEM grid. Comparing the inter-planar distances measured for the crystalline lattices with those values from JCPDS, it was found that these particles are mainly composed of Fe<sub>2</sub>O<sub>3</sub>, while iron carbide was rarely found. The coexistence of FeC suggests that some of the ferrocene was pyrolyzed in the oxygen-deficient region in the flame where the soot particles are normally generated. A co-injection of ferrocene and diesel fuel is likely expected to maximize the contact between catalysts and carbonaceous PM, resulting in an enhancement of the catalytic oxidation of PM.

### 3.2. Effect of ferrocene on the kinetics of PM oxidation

Fig. 4 shows dynamic TGA profiles of all samples at a heating rate of 4 °C min<sup>-1</sup>. When 50 ppm of ferrocene was added, the on-set temperature of PM oxidation decreased by 100 °C. As the mixing level was increased, the oxidation is initiated at the lower temperature, which is consistent with the findings

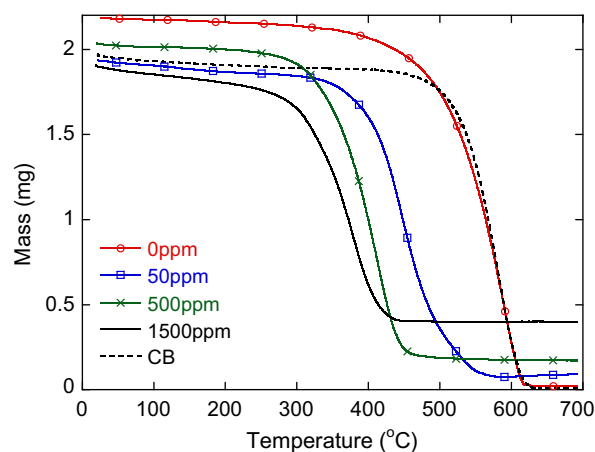


Fig. 4 – Dynamic TGA profiles of carbon black (CB) and 0, 50, 500, and 1500 ppm ferrocene-doped flame soot particles.

of Neeft et al.'s [6] but inconsistent with those of Lahaye et al. [1]. Particularly at 1500 ppm, the on-set temperature decreases to 320 °C, which is close to the exhaust gas temperature of a conventional diesel engine running at a high load. This demonstrates a potential for the natural regeneration of DPF. In addition, the termination of the oxidation process is also advanced to a lower temperature to the extent that the reaction initiation was enhanced. Moreover, the catalytic effect appears to be far more dramatic than ever reported in previous cases of physical mixings [5,6].

The ash content in the PM was estimated by the mass fraction of residue after the oxidation reaction ended.

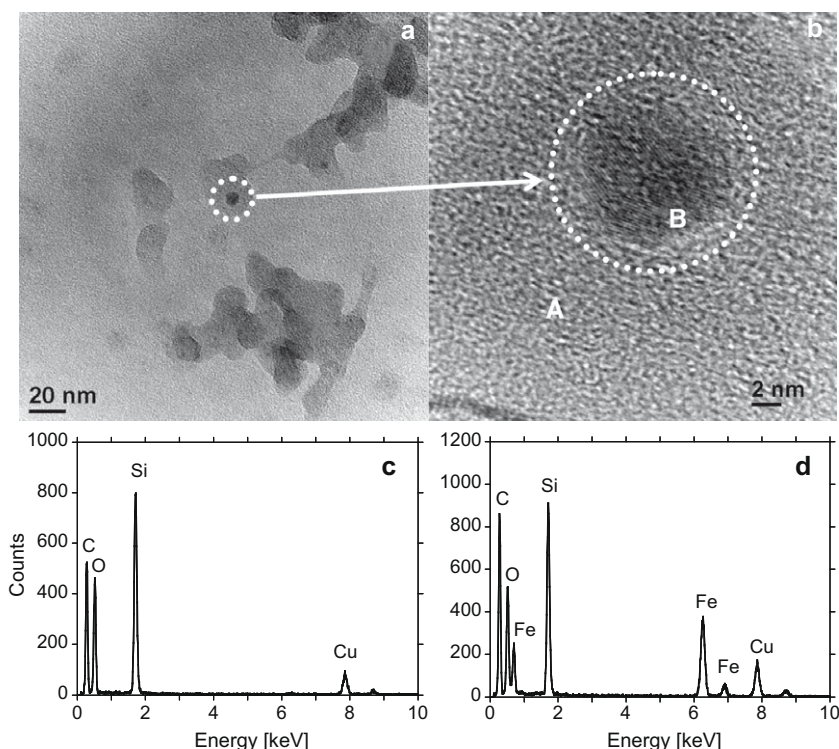


Fig. 3 – TEM image for 50 ppm ferrocene-doped soot particles: (a) at low magnification, (b) a magnified image for the dotted-circular region in (a), (c and d) show EDS spectra for A and B region in (b), respectively.

Fig. 4 shows that the ash content increases from very close to zero to ca. 20% as the content of ferrocene increases to 1500 ppm. The iron content of these catalyzed PM samples were analyzed by ICP-AES and compared with the ash content (see Fig. 5). As the ash content is linearly proportional to the iron content, the ash is likely to be iron compound that are mainly composed of iron oxide coming from the ferrocene.

Calculations of oxidation kinetics of individual sample were made from the following mathematical formation of the dynamic TGA profiles. For a variety of solid-state reactions, the reaction rate of  $dx/dt$  is expressed as a function of the temperature,  $T$ , and the degree of reaction,  $\alpha$ , by [23].

$$\frac{d\alpha}{dt} = k(T)f(\alpha), \quad (1)$$

where  $t$  is the time,  $k(T)$  is the rate constant, and  $f(\alpha)$  is a mathematical function describing the reaction mechanism [23,25]. The value of  $\alpha$  is defined by the relative mass loss of  $(w_0-w)/(w_0-w_f)$ , in which  $w_0$  and  $w_f$  are the initial and final mass of the sample, respectively. The present TGA experiments were conducted at a constant heating rate ( $\beta = dT/dt$ ) of  $4\text{ }^\circ\text{C min}^{-1}$ . An alternative form is more often used:

$$\frac{d\alpha}{dT} = \frac{1}{\beta} k(T) \cdot f(\alpha) \quad (2)$$

Here, the term of  $dx/dT$  is obtained by directly differentiating  $\alpha$  with respect to  $T$  in the TGA profiles in Fig. 4.

A contracting sphere model (see Table 1 of Vyazovkin and Wight [26];  $f(\alpha) = 3(1-\alpha)^{2/3}$ ) is employed to produce  $k(T)$  as a function of  $T$  from Eq. (2). In order to validate the contracting sphere model, a single catalyzed aggregate deposited on a  $\text{SiO}_2$ -coated TEM grid was tracked before and after the partial oxidation process, as shown in Fig. 6(a and b), respectively. Unlike the un-catalyzed biodiesel PM of Song et al. [27], the catalyzed aggregates at a ferrocene dose of 50 ppm appear to be

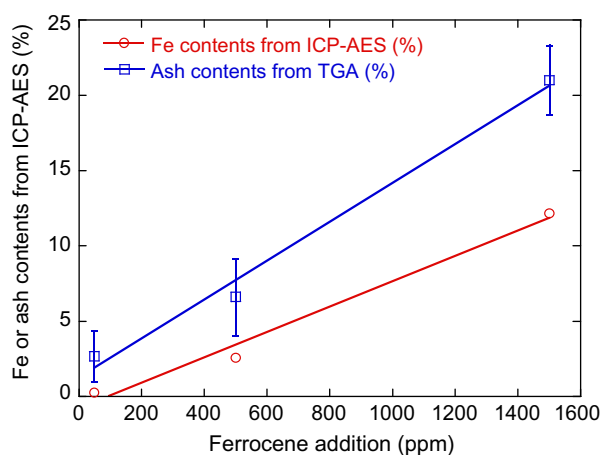


**Fig. 5 – Comparison of iron contents and ash contents of as-received samples generated at different doses of ferrocene; as ferrocene additions increases, iron contents and ash contents are both linearly increased. Under the assumption that the iron exists as a form of oxide, the content of iron oxide is estimated from the ICP-AES data and approaches the ash content obtained from TGA, suggesting that the ash is mainly composed of iron compound or oxide.**

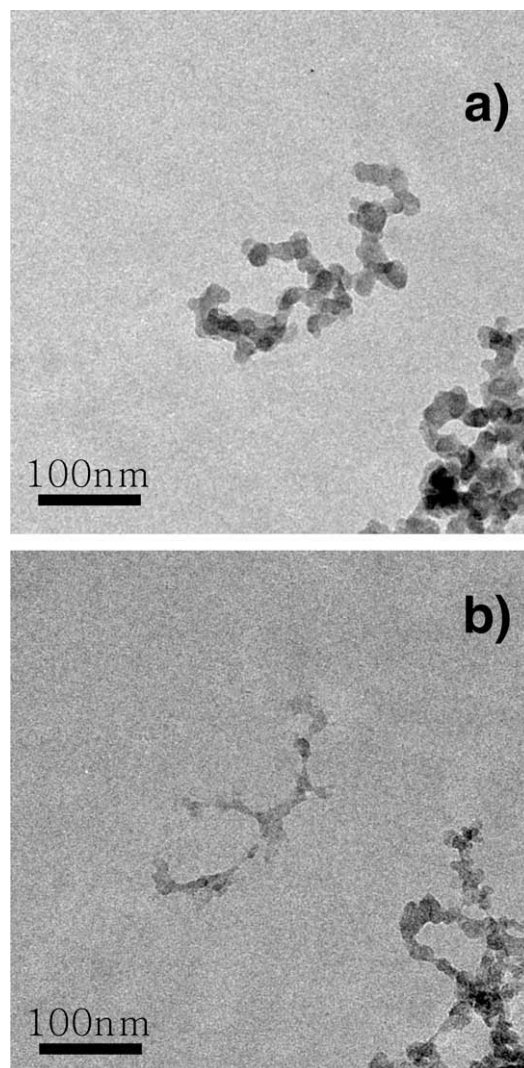


**Fig. 6 – Morphological change of a 50 ppm-doped flame soot aggregate tracked (a) before and (b) after the partial oxidation.**

oxidized from the surface to the inside, with no obvious signature of a hollow structure. This is fairly consistent with the observation of Jung et al. [28] for flame soot oxidation. Hence, the contracting sphere model is more suitable for obtaining the oxidative kinetics at least in the present conditions.

The value of  $k(T)$  is approximated to the Arrhenius form of  $k(T) = A \exp(-E_A/RT)$ , where  $A$  is the pre-exponential factor,  $E_A$  is the activation energy, and  $R$  is the gas constant. Substituting this into Eq. (2), an explicit relationship to obtain  $E_A$  is given by

$$\frac{\beta}{f(\alpha)} \frac{d\alpha}{dT} = k(T) = A \exp\left(-\frac{E_A}{RT}\right). \quad (3)$$

The equation can be restated as

$$\ln\left(\frac{\beta}{f(\alpha)} \frac{d\alpha}{dT}\right) = \ln(A) - \frac{E_A}{RT} \quad (4)$$

Thus, the Arrhenius plot shown in Fig. 7 can be constructed by plotting the left term in Eq. (4) against the reciprocal temperature ( $1/T$ ); the slope indicates the apparent

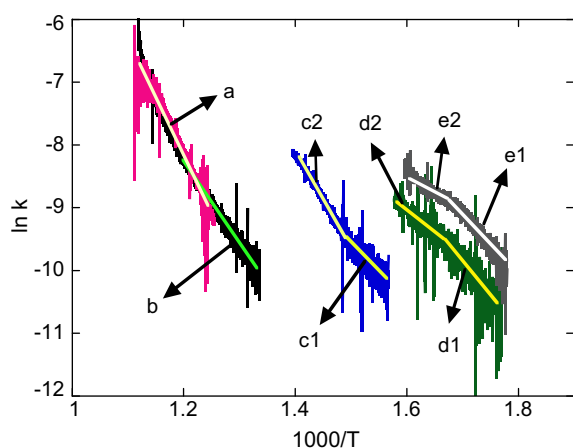


**Fig. 7** – Arrhenius plot of CB and flame soot samples generated at different ferrocene additions. The activation energies corresponding to the arrowed slopes are (a)  $169.1 \text{ kJ mol}^{-1}$  for the CB, (b)  $110.9 \text{ kJ mol}^{-1}$  for 0 ppm-doped sample, (c1)  $74.9 \text{ kJ mol}^{-1}$  for 50 ppm-doped sample, (c2)  $121.6 \text{ kJ mol}^{-1}$  for 50 ppm-doped sample, (d1)  $87.0 \text{ kJ mol}^{-1}$  for 500 ppm-doped sample, (d2)  $64.2 \text{ kJ mol}^{-1}$  for 500 ppm-doped sample, (e1)  $94.7 \text{ kJ mol}^{-1}$  for 1500 ppm-doped sample, and (e2)  $45.8 \text{ kJ mol}^{-1}$  for 1500 ppm-doped sample.

activation energy of the reaction (actually  $-E_A/R$ ) while the y intercept gives  $\ln(A)$ . The term of  $d\alpha/dT$  is considerably fluctuated at a very low-temperature; hence, the data in Fig. 7 is presented only in the range of  $0.1 \leq \alpha \leq 0.9$ , where most of the reaction takes place. Another effort to reduce the uncertainty of low-temperature data is that the temperature-ramping rate was set as low as  $4 \text{ }^\circ\text{C min}^{-1}$  in TGA experiment, which provides more data for fitting in a way to improve the reliability of data.

In a low-temperature range (i.e.,  $250 \text{ }^\circ\text{C} < T < 450 \text{ }^\circ\text{C}$ ), the flame soot shows somewhat higher reactivity with lower activation energy ( $110.9 \text{ kJ mol}^{-1}$ ) compared to the CB. In a higher temperature range (i.e.,  $450 \text{ }^\circ\text{C} < T < 600 \text{ }^\circ\text{C}$ ), however, the flame soot shows reaction behavior that is similar to that of the CB in terms of  $k(T)$  and  $E_A$ . Unlike the CB, the overall oxidation of all flame soot samples seemingly takes place in two

steps, i.e., low-temperature and high-temperature reactions with different activation energies. Upon an increase of the content of ferrocene from 0 to 50, 500, and 1500 ppm, the oxidation kinetics is promoted with a continuous decrease in the high-temperature activation energy ( $E_{A,\text{high}}$ ) from 160 to 121.6, 64.2 and  $45.8 \text{ kJ mol}^{-1}$ , respectively. However, the low-temperature activation energy ( $E_{A,\text{low}}$ ) shows a different behavior; the value of  $E_{A,\text{low}}$  is minimized to  $74.9 \text{ kJ mol}^{-1}$  with 50 ppm of ferrocene, and a further dose of ferrocene begins to increase the value of  $E_{A,\text{low}}$  to  $94.7 \text{ kJ mol}^{-1}$ . This suggests that the fuel-borne catalyst mainly enhances the high-temperature oxidation by lowering the activation barrier. In contrast, the low-temperature oxidation is likely affected by other factors. The rest of this article will be devoted to determining these other factors if they exist.

Table 2 summarizes the activation energies of carbonaceous PM that have been reported to date. The value of  $E_A$  for the present CB ( $169 \text{ kJ mol}^{-1}$ ) agrees fairly well with the values of the literature of  $140\text{--}170 \text{ kJ mol}^{-1}$ . Even in the absence of catalysts, the value of  $E_A$  for diesel PM were widely scattered in the range of  $64\text{--}210 \text{ kJ mol}^{-1}$ , depending on the engine operation parameters and the pretreatment of the

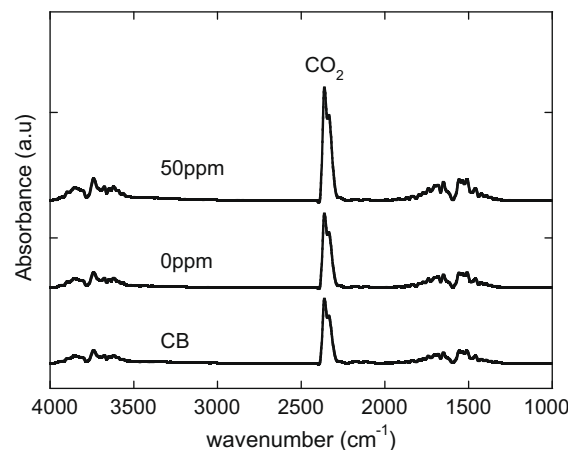


**Fig. 8** – GC-FTIR spectra of evolving gases during oxidation of CB, 0 and 50 ppm-doped flame soot particles.

**Table 2** – Comparisons of activation energies for oxidation reaction of various carbon-based particles in the absence or presence of catalysts from literatures.

References	Origin of the samples	Catalyst	$E_A$ ( $\text{kJ mol}^{-1}$ )	
			Absence of catalyst	Presence of catalyst
Lahaye et al. [1]	Soot	$\text{CeO}_2$	170	120
Stanmore et al. [11]	Diesel PM	$\text{CeO}_2$	210	210
Ciambelli et al. [8]	CB	Cu–V–K	151	100
Du et al. [29]	Soot	Ca	145	120
Bokova et al. [21]	CB	$\text{CeO}_2 + \text{Al}_2\text{O}_3$	163	63
Kim et al. [13]	Soot	$\text{Fe}_2\text{O}_3$	162	116
Jung et al. [30]	Diesel PM	$\text{CeO}_2$	110	102
Yezerets et al. [31]	Diesel PM	–	64–126	–
Smith [32]	Soot	–	142	–
Neeft et al. [2]	CB	–	168	–
Higgins et al. [15]	Diesel PM	–	108–114	–



PM. For un-catalyzed flame soot particles, the  $E_A$  value has been reported to range from 140 to 170  $\text{kJ mol}^{-1}$ . This is consistent with  $E_{A,\text{high}}$  rather than with  $E_{A,\text{low}}$  in Fig. 6. Moreover, Table 2 shows that  $E_A$  is decreased by 10–100  $\text{kJ mol}^{-1}$  in the presence of catalysts. Consistently, Fig. 6 shows that  $E_{A,\text{high}}$  is decreased by 45–115  $\text{kJ mol}^{-1}$  when ferrocene is added in the broad range of 50–1500 ppm.

Particularly at the early stage of oxidation in Fig. 4, the mass loss can be induced by either evaporation of any volatile matter such as the soluble organic fraction (SOF) and moisture or oxidation of the more reactive species. To rule out the contribution of the volatile matter [33], the chemical compositions of the gases that evolved from the samples while

they are heated at 300 °C in air were measured with GC-FTIR. Fig. 8 shows a distinct  $\text{CO}_2$  peak in the GC-FTIR spectra, the intensity of which increases in the sample order of 50 ppm > 0 ppm > CB. At that time, the intensity of the peak at 3500–4000  $\text{cm}^{-1}$ , corresponding to the OH stretching mode of  $\text{H}_2\text{O}$ , is nearly invariant, together with no apparent evidence of the evaporated SOF. A very similar spectrum, but with a significant decrease of peak intensity, was observed from the 50 ppm sample while being heated at 200 °C. Besides, a group of very little peaks appeared at 2750–3100  $\text{cm}^{-1}$  representing aromatic and aliphatic C–H vibration. This suggests that the SOF, even if exists, was in quite a low level. It is also noted that the SOF most likely evaporates

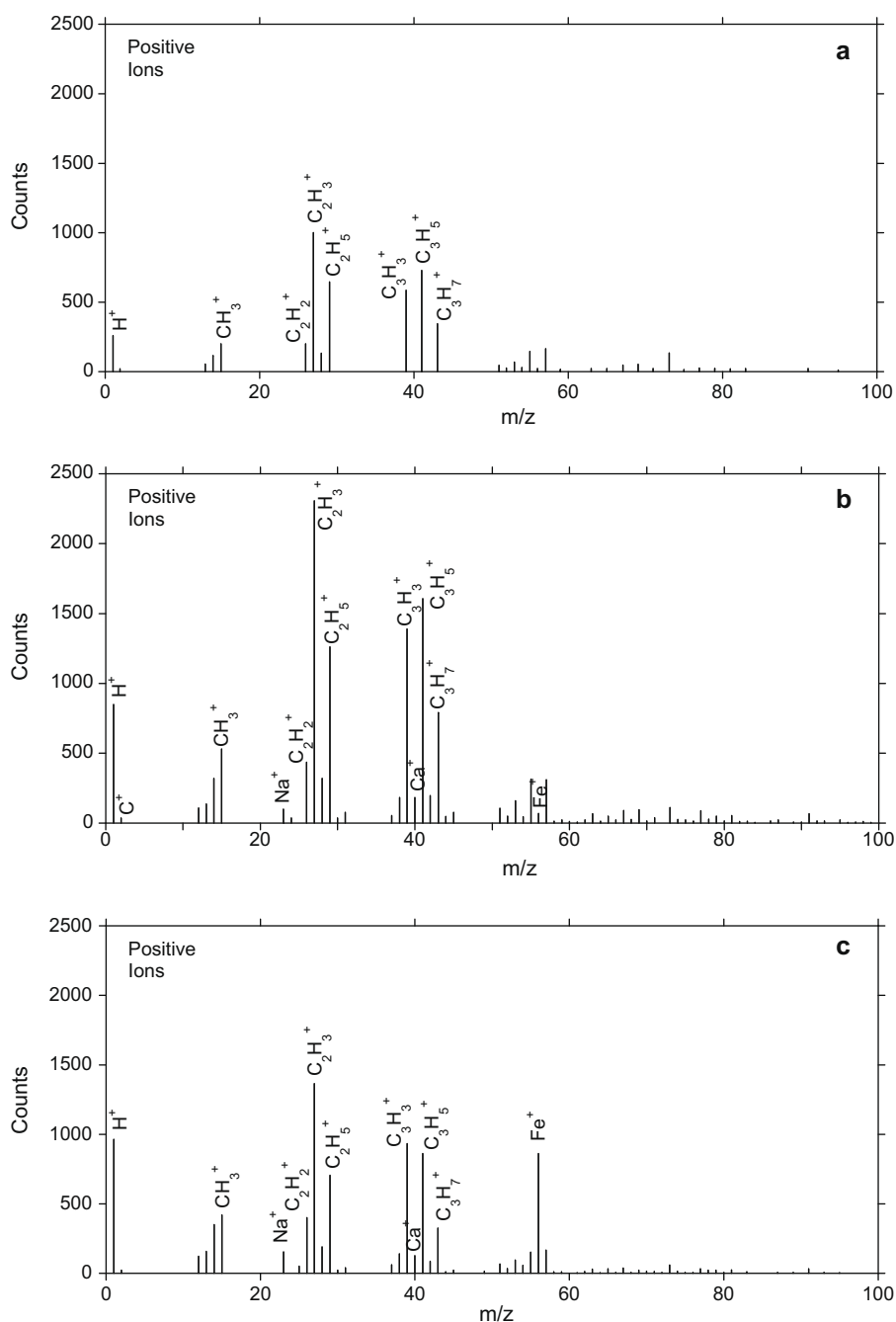


Fig. 9 – Positive SIMS spectra for (a) CB, (b) 0 ppm-doped, and (c) 50 ppm-doped flame soot particles.

rather than oxidizes at such a low-temperature [11] and the temperature range of interest here is higher than 300 °C where the contribution of SOF is negligible. Thus, the low-temperature mass loss is attributed to the oxidation of more reactive species. Of particular interest is to determine whether or not the amount of the more reactive species varies with the doping level and whether it is correlated with the behavior of  $E_{A,low}$ .

### 3.3. Characterization of iron-containing flame soot

Several factors, including the SOC [22,29,30], SOF, and crystalline order of the CGL [27], are thought to affect the oxidation

kinetics of un-catalyzed diesel PM. Song et al. [27] reported that the reaction rate constant was correlated with the SOC but scattered with the other factors of un-catalyzed diesel PM. In their corresponding research [34], however, they suggested that the physical locations of fuel-borne catalysts, i.e., whether remaining at the surface or becoming embedded in graphene layer, were likely the most dominant factor in the catalytic initiation of oxidation. Though they showed that the CGL was mostly invariant irrespective of the existence of the catalyst, the possible effects of the SOC and the SOF were not reported. Therefore, this section of the present study aims to report variations of the SOC, the SOF and the CGL at different

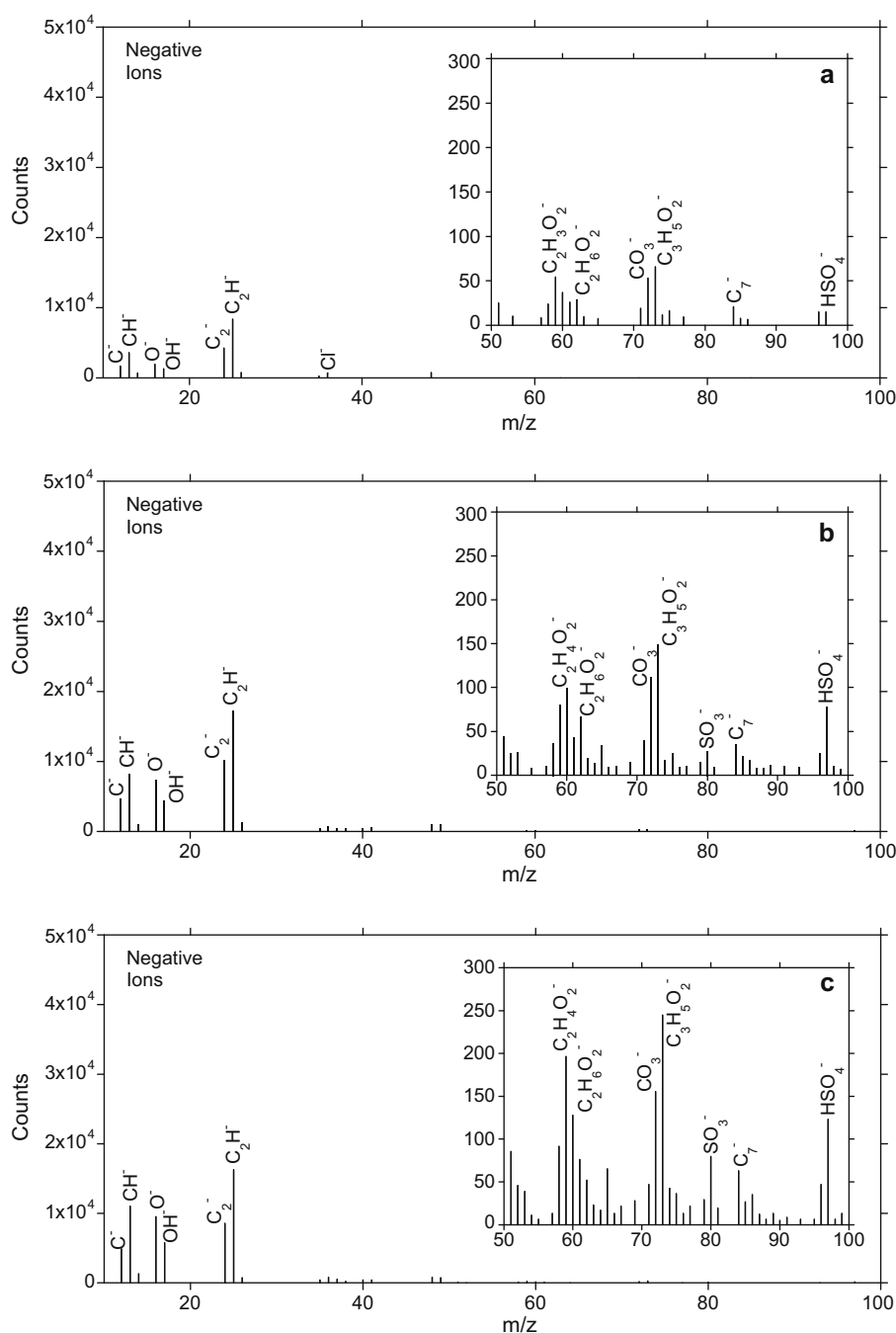


Fig. 10 – Negative SIMS spectra for (a) CB, (b) 0 ppm-doped, and (c) 50 ppm-doped flame soot particles. The inset figures are magnifications of the high  $m/z$  region.

doses of ferrocene and to confirm the impacts of these factors on the reactivity.

SIMS spectra has been used for a qualitative assessment of ionic species concentration [13,35] due to its species-dependent quantum efficiency. However, a peak intensity of a single ion can be used to determine a relative abundance of the ion (or species) content between samples. Fig. 9 shows the positive-ion SIMS spectra of CB, 0 and 50 ppm. The overall characteristics of the spectra are similar to those of diesel PM as observed by Kirchner et al. [35]. Unlike Fig. 9(a) of the CB, Fig. 9(b) shows that the un-catalyzed flame soot contains metallic Na, Ca, and Fe as well as a high level of organics, SOF. At a dose of 50 ppm ferrocene, the iron peak is greatly increased in Fig. 9(c) as compared to Fig. 9(b), as expected. On the other hand, the SOF decreases slightly, which is likely due to the catalytic oxidation of the SOF enhanced by the iron oxide catalyst [7] (also see Fig. 2). It is notable that the alkali metal peaks found only with flame soot samples are mostly invariant regardless of the doping level of ferrocene. This suggests that the alkali metals originate from the diesel fuel itself. Additionally, the alkali metal, known as a catalyst for carbon oxidation [6,29], may partially explain why the un-catalyzed flame soot has a lower activation barrier than the CB in the low-temperature range shown in Fig. 7.

In Fig. 10, the negative-ion SIMS spectra of the same samples are mostly composed of carbon fragments with trace levels of the SOC and fuel-borne sulfur compounds, as highlighted in the inset figure. As compared to the CB in Fig. 10(a), the un-catalyzed flame soot contains a higher level of SOC in Fig. 10(b). Major peaks at  $m/z = 59$  and  $73$ , which are assigned as  $C_2H_4O_2^-$  and  $C_3H_5O_2^-$ , correspond to two sorts of lactones, such as  $\beta$ -propiolactone and  $\gamma$ -butyrolactone, respectively. In addition, the peak at  $m/z = 72$  can be assigned as carbonate. Among a variety of SOCs, the lactone is most unstable. Hence, it can readily decompose into  $CO_2$  at low-temperatures [22]. Interestingly, the lactone intensity increases in the sample order of  $CB < 0 \text{ ppm} < 50 \text{ ppm}$ . A further dose of ferrocene did, however, reduce the lactone again (see Fig. 11). Such a characteristic of a lactone peak is completely consistent with that of the  $E_{A,low}$  characteristics shown in Fig. 7.

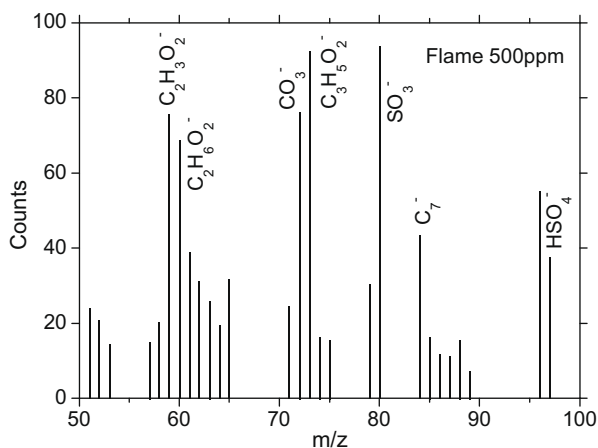


Fig. 11 – Negative SIMS spectrum of the catalyzed soot particles with 500 ppm ferrocene.

Raman spectroscopy can characterize fine structure and short-range order of the carbon framework or defects in a carbon nanotube (CNT) [36]. Three major peaks in the Raman spectra for CNT have been reported: a radial breathing mode

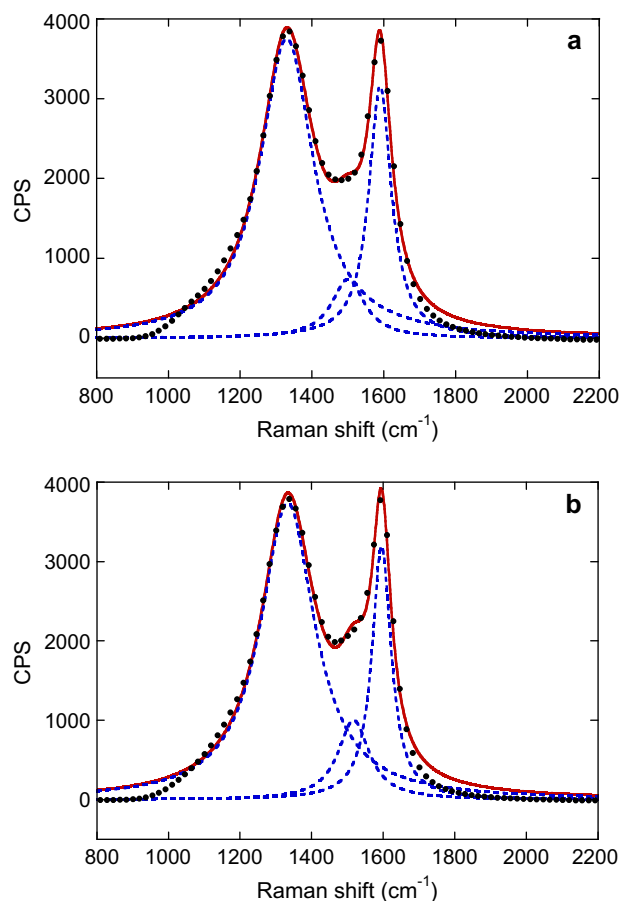


Fig. 12 – Raman spectra for (a) 0 ppm-doped and (b) 50 ppm-doped flame soot particles.

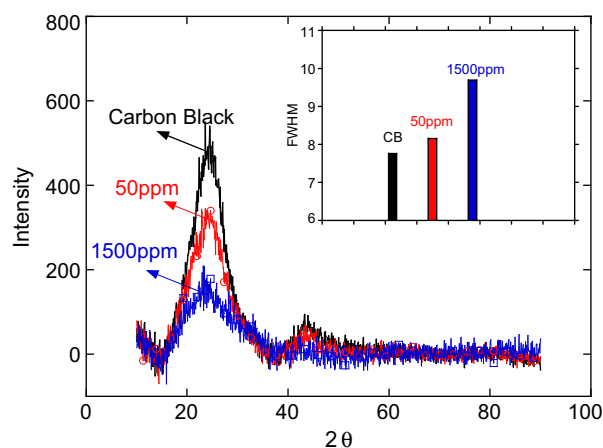


Fig. 13 – XRD spectra for CB, 50 and 1500 ppm-doped flame soot particles. The inset figure shows corresponding variations of the full width at half maximum of (0 0 2) Bragg reflection of carbon.

at  $\leq 400\text{ cm}^{-1}$ , a D band (a stretching mode for C=C bond) at  $1300\text{--}1350\text{ cm}^{-1}$ , and a G band (a tangential mode) at  $1588\text{ cm}^{-1}$ . As CNT oxidation proceeds and the ordered structure of the CNT wall begins to collapse, the G band broadens due to appearance of a new peak at  $1520\text{ cm}^{-1}$  and/or the D band peak likewise increases. The result shows in Fig. 12 that there is no remarkable difference in the peak profiles between the cases of 0 and 50 ppm doping, suggesting that the addition of ferrocene hardly affects the short-range order of the carbon structure.

Likewise, an XRD measurement was taken to note any changes in the long-range order of CB and the 50-ppm and 1500-ppm ferrocene-added samples. Fig. 13 shows that the most prominent peak at  $2\theta = 24^\circ$ , corresponding to the (0 0 2) Bragg reflection of graphite, decreases as the mixing level of ferrocene increases. This is accompanied by significant peak broadening. The inset figure shows that the full width at half maximum (FWHM) of the peak increases noticeably, suggesting a decrease in the crystallite size. The Scherrer equation confirms that the crystallite size decreases with an increase in the mixing level of ferrocene: 1.21 nm of CB, 1.16 nm of 50 ppm, and 0.97 nm of 1500 ppm. This suggests that the long-range order of the carbon structure gradually collapses due to the iron-containing catalysts. This also suggests that the degraded crystalline order of the CGL with the addition of ferrocene partly contributes to the enhancement of the low-temperature reactivity of PM.

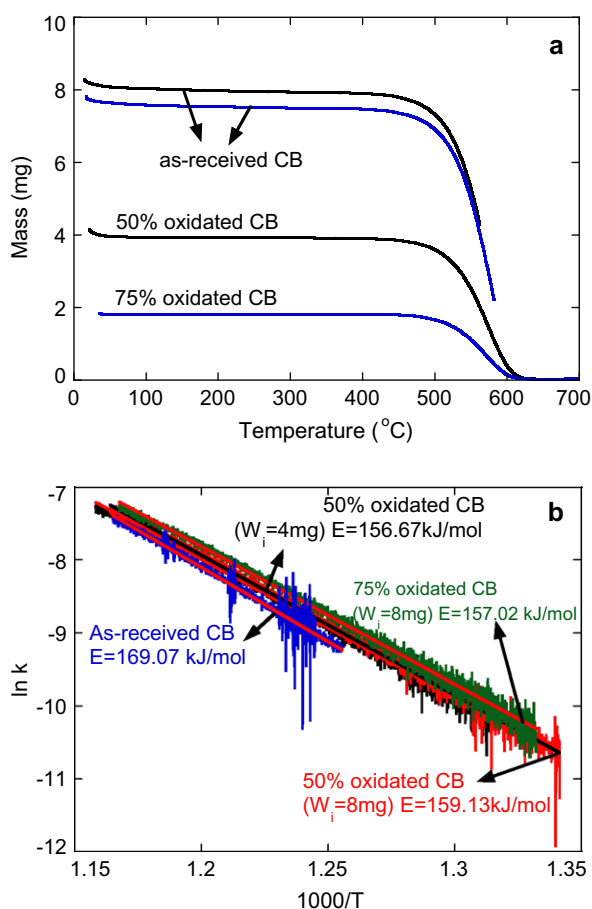


Fig. 14 – (a) TGA curves and (b) Arrhenius plots of CB partially oxidized to 50% and 75%.

#### 3.4. Oxidative characteristics of partially oxidized PMs

A subsequent step clarified whether or not the aforementioned more reactive surface species can affect the apparent reactivity as well as the initiation of the reaction. Initially, each PM sample was partially oxidized up to 50% or 75% with air using a TGA instrument. The samples were then rapidly cooled to room temperature with nitrogen, in an effort to remove the more reactive species from the surface of the PM. The oxidation kinetics of such specifically treated samples was again measured in air with the TGA. It should be noted that only three samples containing higher SOC values, in this case the CB, 0 and 50 ppm-doped samples, were utilized in this stripping-off experiment because the samples with higher doping levels contained a considerably low level of SOC. Figs. 14–16 show the TGA profiles and the corresponding Arrhenius plots of these three samples, respectively.

Fig. 14(b) reveals that the CB undergoes no remarkable changes in its reactivity and  $E_A$  values before and after the partial oxidation. All Arrhenius data fall fairly well on a single straight line, indicating that the value of  $E_A$  is slightly scattered around  $160\text{ kJ mol}^{-1}$ . The un-catalyzed flame soot, however, shows a noticeable increase of  $E_A$  as partial oxidation progresses, as clearly shown in Fig. 15(b). Interestingly, the value of  $E_A$  approaches the value of CB as the surface-reactive species is gradually peeled off. This suggests that the SOC is first consumed at the early stage of oxidation while

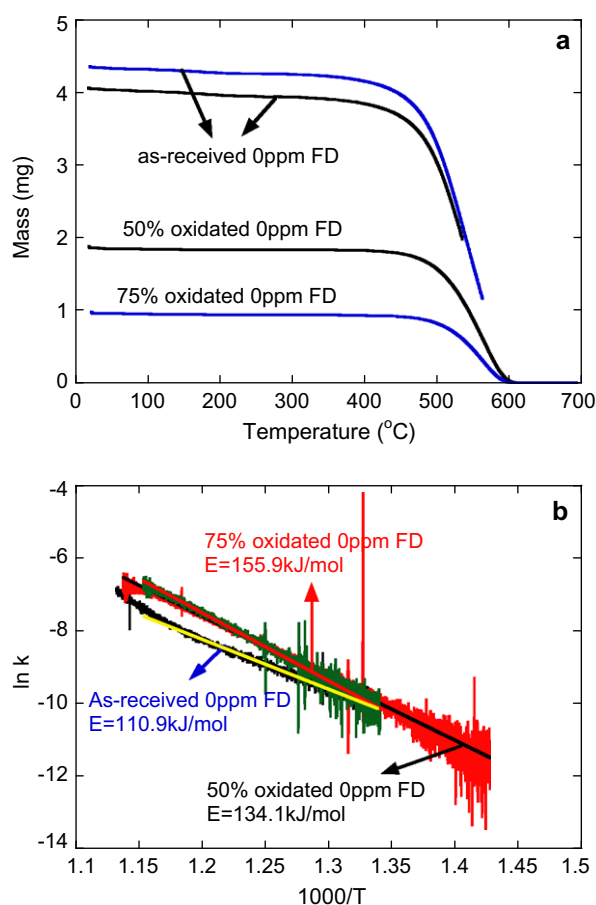
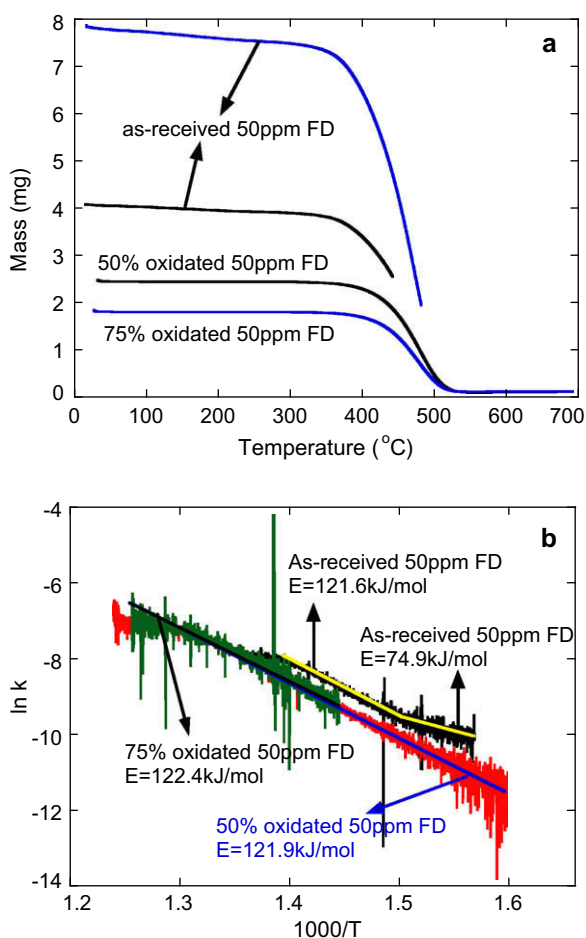


Fig. 15 – (a) TGA curves and (b) Arrhenius plots of un-doped flame soot particles partially oxidized to 50% and 75%.



**Fig. 16 – (a) TGA curves and (b) Arrhenius plots of 50 ppm-doped flame soot particles partially oxidized to 50% and 75%.**

the remaining PM shows oxidative behavior similar to that of the CB.

For the 50 ppm-doped sample, Fig. 16(b) shows that the low-temperature reactive species having an  $E_{A,low}$  value of  $74.9 \text{ kJ mol}^{-1}$  is removed at 50% oxidation; the remaining PM shows a single-step oxidation process in the form of a straight line. In this case, the  $E_A$  value of the pre-oxidized sample is nearly identical to the high-temperature activation energy  $E_{A,high}$  ( $120 \text{ kJ mol}^{-1}$ ) before the surface treatment. This implies that the surface-reactive species mainly enhance the initiation of the reaction at a low-temperature but scarcely affect the high-temperature oxidation. Therefore, the decreased value of  $E_{A,high}$  as the dose of ferrocene increases is presumably due to the catalytic effect of the lattice oxygen of the iron oxide [34], implying that it is mainly responsible for the enhancement in the oxidation shown in Fig. 4. Within 95% confidence level, maximum uncertainty of the activation energy is estimated to less than  $\pm 10 \text{ kJ mol}^{-1}$ . Further evaluation of the two-step approximation is made by simulating TGA curves seen in Fig. 4 with the above Arrhenius parameters. Fig. 17 shows the simulated curves are in good agreements with experimental data for 0, 50, and 500 ppm samples, particularly in most of the reaction zone.

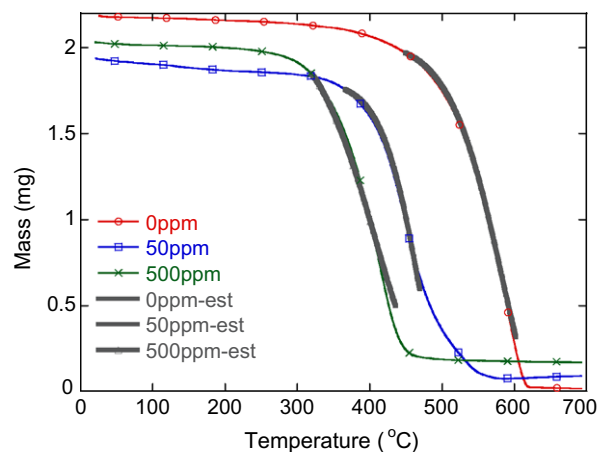


**Fig. 17 – Simulations of thermogravimetric mass loss based on the kinetic data under the two-step reactions.**

#### 4. Conclusions

The findings of this study are summarized as follows. The as-generated catalyzed flame soot particles were characterized in terms of their oxidative reactivity, content of metal oxide, SOC and short-range/long-range order of their CGL. Upon exposing the samples to partial oxidation, catalytic oxidation was noted to take place in two consecutive steps as the temperature increased. In the first step, the initiation of oxidation was affected mainly by the SOC and partly by the long-range crystalline order of the CGL. However, once the catalytic oxidation commenced, the progress of the reaction, as the second step, was mainly determined by the added amount of ferrocene, which was accompanied by a remarkable change in the activation energy. Finally, by tracking the morphology of a single soot agglomerate before and after partial oxidation by TEM, it was verified that contracting sphere model was suitable for the present study.

#### Acknowledgments

This work was done as part of the projects “Development of Partial Zero Emission Technology for Future Vehicle” funded by Ministry of Commerce, Industry and Energy, and also supported by Pusan Clean Coal Center Research Grant. We are grateful for their financial supports.

#### REFERENCES

- [1] Lahaye J, Boehm P, Chambrion P, Ehrburger P. Influence of cerium oxide on the formation and oxidation of soot. *Combust Flame* 1996;104(1–2):199–207.
- [2] Neef JPA, Nijhuis TX, Smakman E, Makkee M, Moulijn JA. Kinetics of the oxidation of diesel soot. *Fuel* 1997;76(12):1129–36.
- [3] Mayer A. VERT: diesel nano-particulate emissions: properties and reduction strategies. SAE (980539); 1998.
- [4] Vincent MW, Richards PJ, Dementhon JB, Martin B. Improved diesel particulate filter regeneration performance using fuel soluble additives. SAE (1999-01-3562); 1999.

- [5] Neeft JPA, Makkee M, Moulijn JA. Catalysts for the oxidation of soot from diesel exhaust gases. I. An exploratory study. *Appl Catal B* 1996;8(1):57–78.
- [6] Neeft JPA, Makkee M, Moulijn JA. Catalytic oxidation of carbon black-I. Activity of catalysts and classification of oxidation profiles. *Fuel* 1998;77(3):111–9.
- [7] Neri G, Bonaccorsi L, Donato A, Milone C, Musolino MG, Visco AM. Catalytic combustion of diesel soot over metal oxide catalysts. *Appl Catal B* 1997;11(2):217–31.
- [8] Ciambelli P, d'Amore M, Palma V, Vaccaro S. Catalytic combustion of an amorphous carbon black. *Combust Flame* 1994;99(2):413–21.
- [9] Setzer G, Schutz W, Schuth F. Transition metal compound oxide catalysts for lowering the light-off temperature of particles from diesel exhaust. In: *Proceedings 10th international congress on catalysis*. Amsterdam, Budapest, Hungary: Elsevier; 1993. p. 2629–32.
- [10] Lahaye J, Boehm P, Ehrburger P. Metallic additives in soot formation and post-combustion. In: *Soot formation in combustion: mechanisms and models*. Berlin: Springer; 1994. p. 307–15.
- [11] Stanmore B, Brilhac JF, Gilot P. The ignition and combustion of cerium-doped diesel soot. *SAE (1999-01-0115)*; 1999.
- [12] Bonnefoy F, Gilot P, Stanmore BR, Prado G. A comparative study of carbon black and diesel soot reactivity in the temperature range 500–600 °C: effects of additives. *Carbon* 1994;32(7):1333–40.
- [13] Kim SH, Fletcher RA, Zachariah MR. Understanding the difference on oxidative properties between flame and diesel soot nanoparticles: the role of metals. *Environ Sci Technol* 2005;39(11):4021–6.
- [14] Kasper M, Siegmann K, Sattler K. The influence of fuel additives on the formation of carbon during combustion. *J Aerosol Sci* 1999;30(2):217–25.
- [15] Higgins KJ, Jung H, Kittelson DB, Roberts JT, Zachariah MR. Kinetics of diesel nanoparticle oxidation. *Environ Sci Technol* 2003;37(9):1949–54.
- [16] Lee D, Miller A, Kittelson DB, Zachariah MR. Characterization of metal-bearing diesel nanoparticles using single-particle mass spectrometry. *J Aerosol Sci* 2006;37(1):88–110.
- [17] Lee D, Choi M. Coalescence enhanced synthesis for nanoparticles to control size, morphology and crystalline phase at high concentrations. *J Aerosol Sci* 2002;33(1):1–16.
- [18] Setiabudi A, Makkee M, Moulijn JA. The role of NO<sub>2</sub> and O<sub>2</sub> in the accelerated combustion of soot in diesel exhaust gases. *Appl Catal B-Environ* 2004;50:185–94.
- [19] Uner D, Demirkol MK, Dernaika B. A novel catalyst for diesel soot oxidation. *Appl Catal B-Environ* 2005;61:334–45.
- [20] Reddy BM, Rao KN. Copper promoted ceria-zirconia based bimetallic catalysts for low temperature soot oxidation. *Catal Commun* 2009;10(9):1350–3.
- [21] Bokova MN, Decarne C, Abi Aad E, Pryakhin AN, Lunin VV, Aboukais A. Kinetics of catalytic carbon black oxidation. *Thermochim Acta* 2005;428(1):165–71.
- [22] Mul G, Neeft JPA, Kapteijn F, Moulijn JA. The formation of carbon surface oxygen complexes by oxygen and ozone: the effect of transition metal oxides. *Carbon* 1998;36(9):1269–76.
- [23] Mahadevan R, Lee D, Sakurai H, Zachariah MR. Measurement of condensed-phase reaction kinetics in the aerosol phase using single particle mass spectrometry. *J Phys Chem A* 2002;106(46):11083–92.
- [24] Lee EJ, Oh KC, Shin HD. Soot formation in inverse diffusion flames of diluted ethane. *Fuel* 2005;84(5):543–50.
- [25] Ettarh C, Galwey AK. Thermal analysis of anhydrous mixtures of calcium nitrate and selected metal oxides. *Thermochim Acta* 1995;261:125–39.
- [26] Vyazovkin S, Wight CA. Isothermal and non-isothermal kinetics of thermally stimulated reactions of solids. *Int Rev Phys Chem* 1998;17:407–33.
- [27] Song J, Alam M, Boehman AL, Kim U. Examination of the oxidation behavior of biodiesel soot. *Combust Flame* 2006;146(4):589–604.
- [28] Jung H, Kittelson DB, Zachariah MR. Kinetics and visualization of soot oxidation using transmission electron microscopy. *Combust Flame* 2004;136(4):445–56.
- [29] Du Z, Sarafim AF, Longwell JP. Activation energy in temperature-programmed desorption: modelling and application to the soot-oxygen system. *Energy Fuels* 1990;4(3):296–302.
- [30] Jung H, Kittelson DB, Zachariah MR. The influence of a cerium additive on ultrafine diesel particle emission and kinetics of oxidation. *Combust Flame* 2005;142(3):276–89.
- [31] Yezerets A, Currier NW, Eadler HA. Experimental determination of the kinetics of diesel soot oxidation by O<sub>2</sub>-modeling consequences. *SAE (2003-01-1833)*; 2003.
- [32] Smith IW. The intrinsic reactivity of carbons to oxygen. *Fuel* 1978;57(7):409–14.
- [33] Li C, Minh CL, Brown TC. Kinetics of CO and CO<sub>2</sub> evolution during the temperature-programmed oxidation of coke deposited on cracking catalysts. *J Catal* 1998;178(1):275–83.
- [34] Song J, Wang J, Boehman AL. The role of fuel-borne catalyst in diesel particulate oxidation behavior. *Combust Flame* 2006;146(4):73–84.
- [35] Kirchner U, Vogt R, Natzeck C, Goschnick J. Single particle MS, SNMS, SIMS, XPS and FTIR spectroscopic analysis of soot particles during AIDA campaign. *J Aerosol Sci* 2003;34(10):1323–46.
- [36] Osswald S, Flahaut E, Gogotsi Y. In situ Raman spectroscopy study of oxidation of double- and single-wall carbon nanotubes. *Chem Mater* 2006;18(6):1525–33.